Journal of Power Sources 185 (2008) 717–726

Contents lists available at ScienceDirect

Journal of Power Sources

journal homepage: www.elsevier.com/locate/jpowsour

New nanostructured carbons based on porous cellulose: Elaboration, pyrolysis and use as platinum nanoparticles substrate for oxygen reduction electrocatalysis

Elodie Guilminot[a], Roxane Gavillon[b], Marian Chatenet[a,*], Sandrine Berthon-Fabry[c], Arnaud Rigacci[c], Tatiana Budtova[b]

[a] Laboratoire d'Electrochimie et de Physicochimie des Matériaux et des Interfaces (LEPMI)[1], UMR 5631 CNRS-Grenoble INP-UJF, 1130 rue de la Piscine, BP 75, 38402 Saint Martin d'Hères Cedex, France
[b] MINES ParisTech, Centre de Mise en Forme des Matériaux (CEMEF)[2], UMR CNRS 7635, rue Claude Daunesse, BP 207, 06904 Sophia Antipolis Cedex, France
[c] MINES ParisTech, Centre Énergétique et Procédés (CEP), CNRS FRE 2861, BP 207, 1 rue Claude Daunesse, 06904 Sophia-Antipolis, France

ARTICLE INFO

Article history:
Received 7 April 2008
Received in revised form 11 July 2008
Accepted 3 August 2008
Available online 22 August 2008

Keywords:
Porous cellulose
Supercritical drying
Pyrolysis
Nanostructured carbonized aerocellulose
Platinum nanoparticles
PEMFC

ABSTRACT

New nanostructured carbons have been prepared from pyrolysis of recently developed highly porous cellulose, aerocellulose (AC). Aerocellulose is an ultra-light and highly porous pure cellulose material prepared from cellulose gels followed by drying in carbon dioxide supercritical conditions. The carbonized aerocellulose (CAC) materials were obtained after pyrolysis of the aerocellulose under nitrogen flow at 830 °C, and subsequently *doped* by platinum nanoparticles. The platinum insertion process consisted of (i) thermal activation at various temperatures in CO_2 atmosphere, (ii) impregnation by $PtCl_6^{2-}$ and (iii) platinum salt chemical reduction. The aerocellulose materials and their carbonized counterparts were investigated by scanning and transmission electron microscopy (SEM and TEM), mercury porosimetry and thermogravimetric analysis. The morphology of the platinum particles deposited on the carbonized aerocellulose materials (Pt/CAC) was investigated by transmission electron microscopy (TEM) and X-ray diffraction (XRD): the Pt particles are of 4–5 nm size, mainly agglomerated, as a result of the complex surface chemistry of the CAC. Their electrocatalytic activity was investigated by quasi-steady-state voltammetry in the rotating disk electrode (RDE) setup, regarding the oxygen reduction reaction (ORR). The Pt/CAC materials exhibit ORR specific activities comparable with those of commercial Pt/Vulcan XC72R. Their mass activity is lower, as a result of the *ca.* 10 times smaller specific area of platinum as compared with the commercial electrocatalyst. We nevertheless believe that provided an appropriate pyrolysis temperature is chosen, such *green* carbonized aerocellulose could be a promising electrocatalyst support for PEM application.

1. Introduction

With the growing interest for clean energies, many laboratories nowadays focus on the development of proton exchange membrane fuel cell (PEMFC), thanks to its potential interest regarding the reduction of emission of greenhouse gases (provided renewable fuels are used). However, despite such apparent concern of the research community about ecological energy production systems, very few PEFMC electrode materials are indeed *green* materials. For example, the current PEMFC electrocatalysts consist of platinum nanoparticles deposited onto high-area carbon black particles (e.g. 250 $m^2\ g^{-1}$ for Vulcan XC72) [1]. Carbon blacks usually originate from the fossil fuel industry (aromatic oils, natural gas, acethylene) and various processes of thermal oxidizing decomposition (furnace, lamp, channel) or thermal decomposition (acethylene or plasma). Presently, 95% of the production originates from the (incomplete) furnace decomposition of fossil fuels, yielding severe production of CO_2, NO_2, H_2S and CO. In addition, the process efficiency is low (*ca.* 30% effective carbon conversion), despite the high temperatures used 1100–1600 °C, themselves inducing high energy consumption [2]. Since 15 years, carbon aerogels (CA) have been evaluated as high-area carbon substrate; these nanoporous and nanostructured materials are likely produced via a sol–gel process followed

* Corresponding author. Tel.: +33 476 82 65 88; fax: +33 476 82 67 77.
E-mail address: Marian.Chatenet@lepmi.inpg.fr (M. Chatenet).
[1] LEPMI is a member of the Coordination Action for Research on Intermediate and high temperature Membrane-electrode Assemblies (CARISMA), www.carisma-network.eu.
[2] CEMEF is a member of the European Polysaccharide Network of Excellence (EPNOE), www.epnoe.eu.

0378-7753/$ – see front matter © 2008 Elsevier B.V. All rights reserved.
doi:10.1016/j.jpowsour.2008.08.030

by supercritical drying, yielding organic aerogels which are further pyrolyzed into CA at temperatures typically below 1100 °C, which involves smaller energy consumption. Carbon aerogels from the resorcinol–formaldehyde (RF) systems, first synthesized by Pekala, display high electronic conductivities and high surface area [3] as well as sizeable porosity: CA with high mesoporous and low microporous volumes can be tailored on demand [4–6], which render them adapted for electrochemical applications, like fuel cell electrodes materials [7–10]. We recently showed that Pt-doped carbon aerogels (Pt/CA) may display better electrochemical activity than commercial or home-made Pt-doped carbon blacks [11]. Other more *environment-friendly* carbon aerogel precursors were recently considered for use as PEMFC materials [12,13], like cellulose acetate aerogels [14–16].

In this paper, we present the first results on using a recently developed highly porous pure cellulose material, so-called aerocellulose (AC) [17,18], in the carbonized form (carbonized aerocellulose, CAC), as a support material in PEMFC. What we want to present here is firstly, the new materials: carbonized aerocellulose, and their elaboration procedure and secondly, their potential as platinum nanoparticles substrate for oxygen reduction electrocatalysis. We provide a comprehensive study of the elaboration of the Pt/CAC materials starting from the preparation of aerocellulose from cellulose–sodium hydroxide solution, followed by its supercritical CO_2 drying and subsequent pyrolysis, and finally the deposition of platinum nanoparticles onto the CAC surface. The physicochemical properties of the AC, CAC and Pt/CAC materials were investigated using scanning or transmission electron microscopy (SEM and TEM, respectively), X-ray diffraction (XRD), thermogravimetric analysis (TGA), mercury porosimetry and elemental analysis. The electrochemical properties of the Pt/CAC materials, e.g. the active area of deposited platinum (S_{Pt}) and the oxygen reduction reaction (ORR) electroactivity, were determined from CO_{ad}-stripping coulometry and quasi-steady-state ORR voltammetry, respectively, in the classical rotating disk electrode (RDE) setup [19,20].

2. Experimental

2.1. Materials for the elaboration of aerocellulose and carbonized aerocellulose

Cellulose used was microcrystalline Avicel® PH-101, degree of polymerization 180, purchased from FMC (noted as *cellulose* in the following). NaOH was of 97% purity, purchased from VWR. Acetone of analytical grade (99.9%) was purchased from Fisher Bioblock. Distilled water was used for the preparation of solutions. The concentrations are given in wt%.

CO_2 (industrial grade, Air Liquide) was used for the drying of aerocellulose precursors in supercritical conditions, while nitrogen (4N5, Air Liquide, France) and argon (U, Air Liquide) were used for the aerocellulose pyrolysis and the TGA analyses, respectively. High-purity CO (N45, Alphagaz), O_2 and Ar (N45, Messer) gases were used for the electrochemical characterizations.

$NaBH_4$, H_2SO_4 and H_2PtCl_6 products were used in the Merck Suprapur quality for the Pt/CAC elaboration procedure. Isopropanol was purchased from Aldrich for the Pt/CAC ink preparation.

2.2. Physical characterization techniques

2.2.1. Scanning and transmission electron microscopy

SEM pictures of the AC and CAC were kindly provided by Fraunhofer Institute for Applied Polymer Research (FhG-IAP), Postdam, Germany, using a scanning electron microscope model JSM 6330JEOL F at an acceleration voltage of 5 kV.

The TEM images for the AC and platinum-free CAC were made in CEMEF with a PHILIPS CM12 transmission electron microscope at an acceleration voltage of 120 kV. The AC or its pyrolyzed counterpart (CAC) was deposed on a copper grid. The grid was then placed into the chamber through an airlock and bombarded with a focused electron beam.

TEM and high-resolution (HR)-TEM images were also obtained at the Consortium des Moyens Technologiques Communs, CMTC, Grenoble, for the Pt/CAC electrocatalysts on a Jeol 2010 apparatus equipped with a LaB_6 filament, at an acceleration voltage of 200 kV.

2.2.2. X-ray diffraction

X-ray diffraction patterns were recorded for the Pt/CAC electrocatalyst using a Siemens D500 (Bragg-Brentano configuration) using a Cu Kα source operating at 40 kV and 30 mA. The 2θ angle was varied from 20° to 130° using an equivalent step size of 0.067° and accumulating data for *ca.* 60 s per step. The Pt crystallite size was determined using the well-known Scherrer equation for the reflections of the (1 1 1), (2 2 0) and (2 2 2) diffraction peaks of the Pt face-centered cubic lattice. For this purpose, we determined the integral width of each diffraction peak, and corrected the obtained value by the instrumental width of the equipment (*ca.* 0.00105 rad). For each sample, the crystallite diameters presented in the text were averaged for the reflections of the (1 1 1), (2 2 0) and (2 2 2) diffraction peaks.

2.2.3. Porosity measurements

Mercury (Hg) porosimetry measurements were performed on a Micromeritics Autopore IV porosimeter by SAFT, Bordeaux, France. This technique is based on the fact that mercury has a high surface tension, 485 mN m^{-1} and is a strongly non-wetting liquid for most substrates. The pore size distribution was determined from the mercury intrusion data, i.e. the volume of mercury penetrating the pores versus the applied pressure *P*. Under the assumption that all pores are cylindrical, the pore diameter, *D*, calculated from the value of *P* using a well-known Laplace–Washburn capillary law (Eq. (1)):

$$D = 4\gamma \left(\frac{1}{P}\right) \cos\theta \quad (1)$$

where γ and θ denote the surface tension of mercury and the contact angle of mercury (arbitrary taken at 130°) with the sample, respectively. The value of 130° origins from the pioneering work of Orr and Dallavalle in 1959 [21] who considered it as an average for all materials. A more recent recommendation of IUPAC is 141° [22]. For Groen et al. [23], contact angles may vary between 125° and 160°, according to the material and its hydrophilicity. For pure carbon (graphene) 150° should be chosen. As it will be shown in Section 3.4, our materials are not very graphitized and rather hydrophilic, we thus arbitrarily have chosen 130°.

2.2.4. FTIR characterization of the raw and activated CAC samples

The activated and raw (not activated) CAC chemical surface groups were investigated by Fourier Transformed InfraRed (Nicolet 710 spectrometer) spectroscopy before platinum insertion. For this purpose, we mixed 1 mg CAC powder with 500 mg of KBr in an agate mortar; the resulting mixture was pressed successively at 5 tons for 3 min and at 10 tons for 3 min, so as to obtain a pellet. The FTIR spectra, recorded between 4000 and 225 cm^{-1} at 4 cm^{-1} resolution, were averaged over 100 scans.

2.3. Preparation of aerocellulose

A detailed description of aerocellulose preparation and morphology is given in Refs. [17,18]. Here we briefly remind

the main preparation steps putting the accent on details that influence the properties of carbonized aerocellulose. First, cellulose–NaOH–water solutions were prepared by mixing Avicel® with 7.6% NaOH–water solution at −6 °C and stirring at a rate of 1000 min^{-1} for 2 h. Cellulose concentration was of *ca.* 5 wt%. Then, the solution was poured into a cylindrical mould (*ca.* 30-mm height and 10–15-mm diameter) and kept at 50 °C for 2 h. In these conditions, the cellulose–NaOH–water solutions are gelling irreversibly [24]. The resulting cylindrical gels were ready for further treatment.

The next step was the cellulose regeneration. Regenerating the cellulose consists of replacing cellulose solvent, 7.6% NaOH–water solution, by a non-solvent, water in our case. For this purpose, cellulose–NaOH–water gels were placed into a water bath at 50 °C. A phase separation occurs and, as a result, a swollen-in-water cellulose "network" is formed, the sample keeping its initial shape. The first sample (AC1) was regenerated in distilled water, whereas the second (AC2) was regenerated in tap water, in order to check whether this simplification influences or not the final properties of carbonized sample.

The third step consists of drying the regenerated swollen-in-water cellulose. In order to prevent pore collapsing because of the existence of capillary pressure gradient appearing in the pores due to formation of a liquid–vapor meniscus if gels are dried by evaporation, we performed a supercritical drying [25,26]. CO_2 was the solvent used because of its low critical temperature (31.1 °C) and mild critical pressure (73.8 bar) [27,28]. Before drying, water was exchanged with acetone, a fluid that is soluble both in supercritical CO_2 and liquid water. Acetone–swollen cellulose cylinders were obtained after water/acetone exchange and washed in an autoclave with CO_2 in supercritical conditions until all the interstitial acetone was recovered. The system was then slowly and isothermally depressurized down to atmospheric pressure and cooled down to room temperature (see details on drying in supercritical conditions in Ref. [25]).

After drying, pure and white-colored aerocellulose cylinders were extracted from the autoclave at room temperature. The porosity and morphology of the aerocellulose samples will be given in Section 3, in comparison with those for the carbonized samples.

2.4. Pyrolysis of aerocellulose

Prior to pyrolysis, we investigated the aerocellulose thermal behavior by thermogravimetric analysis (TGA) and differential thermal analysis (DTA) to determine the appropriate pyrolysis heating regime. The measurement of aerocellulose weight loss upon heating was performed on a Netzsch STA 409 PC instrument computer-controlled using Proteus Thermal Analysis software. The initial weight of aerocellulose sample was about 20 mg. Two procedures have been used. In the first one, the sample was first heated to 40 °C and kept at this temperature for 0.5 h under primary vacuum and then for 1.5 h under argon flow (20 mL min^{-1} on the quartz crystal microbalance + 60 mL min^{-1} on the sample), in order to expel the adsorbed water. After the mass stabilization, it was heated with a heating rate of 2 °C min^{-1} from 40 to 1200 °C in the 80 mL min^{-1} argon gas flow. In the second procedure, the aerocellulose was heated from room temperature to 1200 °C in a single monotonous temperature ramp of 2 °C min^{-1}, also under 80 mL min^{-1} argon gas flow (Fig. 1). For both procedures, the data were corrected from a benchmark measurement using an empty sample crucible, while a reference containing *ca.* 20 mg Al_2O_3 was heated together with the aerocellulose. As it will be shown in Section 3, the procedure of aerocellulose heating practically does not influence its final weight loss. Thus the samples were eventually pyrolyzed without isothermal step at low temperature.

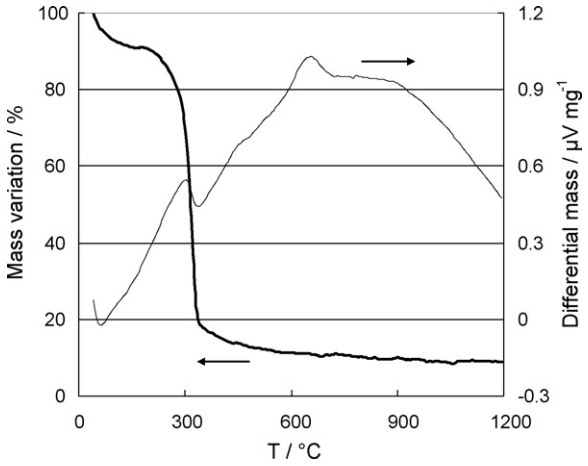

Fig. 1. TGA and DTA of aerocellulose performed following the second procedure (see details in the text): from 20 to 1200 °C at 2 °C min^{-1} under 80 mL min^{-1} Ar flow.

The aerocellulose samples were pyrolyzed using a laboratory furnace under nitrogen atmosphere, with a flow of 5 L min^{-1}. We used a reference carbon sample inside the furnace, the mass of which did not change upon pyrolysis, thus guarantying the absence of leaks during the process. A constant gas flow was chosen to reasonably flush the pyrolysis-exhausted gas, in order to limit carbon oxidation by the oxygen contained in the sample. The temperature was controlled by a thermocouple located near the sample; the sample temperature lies about 20 °C below the set temperature at the plateaus. The pyrolysis cycle consisted of (i) a heating ramp of 2 °C min^{-1} from ambient temperature to 330 °C (which is just above the temperature of the major weight loss, see Fig. 1), then (ii) a stationary plateau of 2 h at 330 °C, followed by (iii) a second heating ramp of 2 °C min^{-1} up to 830 °C (this temperature being chosen because the pyrolysis process seems to be finished above 700 °C, see Fig. 1), followed by (iv) a plateau of 4 h at 830 °C, and finally (v) cooling down to the ambient temperature by thermal inertia under nitrogen flow. The slow heating ramp (2 °C min^{-1}) of such pyrolysis cycle was chosen to prevent the creation of any temperature gradient inside the sample, so as to obtain homogeneous structure and composition throughout the whole sample. The long isothermal step at 830 °C aimed at obtaining a clean (free from carbon oxide groups) carbon surface [29,30] for the carbonized aerocellulose.

2.5. Carbonized aerocellulose activation

The CAC samples obtained after pyrolysis (see Section 2.4) were heat-treated to be used as substrate for platinum nanoparticles deposition. The samples were first finely grounded and then activated in CO_2 atmosphere at 700, 800 or 900 °C during 1 h (as well as 2 h for 800 °C) and gently cooled down to ambient temperature during 1 h under a CO_2 stream.

2.6. Platinum salt insertion and reduction onto CAC

The impregnation step was done immediately after activation, suspending 50 mg grounded CAC powder in a water–isopropanol solution containing H_2PtCl_6, as described in Ref. [15] (the platinum loading was targeted as 20 wt%, i.e. $m_{Pt}/(m_{Pt} + m_{CAC}) = 0.2$). After impregnation, the platinum salt was chemically reduced, directly pouring an excess amount (typically 4×) of $NaBH_4$ in the impregnation solution, under ultrasonic stirring. The Pt-impregnated CAC was then thoroughly washed with 500 mL boiling water and filtered to remove the unreduced platinum salt (which has been observed

Table 1
Weight loss of aerocellulose as a function of temperature from TGA for two procedures used (see details in the text)—A: sample dried under vacuum for 2 h at 40 °C isothermal step; B: monotonous temperature increase

Temperature range (°C)	20–40	40	40–180	180–330	330–700	700–1200	Total
Weight loss A (%)	–	6.8	0	71.0	8.5	1.4	87.7
Weight loss B (%)	0	–	8.9	72.2	8.1	1.8	91

for highly loaded Pt/carbon materials [31]) and boron-containing species (mainly boric acid [11]), and dried by evaporation at 50 °C. Such reduced and cleaned materials are labeled Pt/CAC.

2.7. Electrochemical characterization of Pt/CAC

In order to characterize Pt/CAC electrochemical activity, an active layer was prepared, as described in Refs. [11,15]. It contained *ca.* 91 μg Pt/CAC composed of 18 μg Pt, 73 μg of CAC and *ca.* 30 wt% Nafion®. We considered the Pt/CAC loading was equal to that targeted after impregnation/reduction of the $PtCl_6^{2-}$ salt; such loading was used for the mass activity (MA) calculations.

The experiments were carried out on a rotating disk electrode (EDT 101, Tacussel) setup in 1 M sulfuric acid at room temperature (20 ± 3 °C). The electrochemical cell was connected to a potentiostat PAR 273 (EG&G) with a Pt counter electrode and a saturated calomel electrode (SCE, +0.245 V vs. reference hydrogen electrode, RHE) as reference. All the potentials are nevertheless expressed on the RHE scale.

The active area of platinum was determined from CO_{ad}-stripping coulometry after 3–5 min of CO-bubbling, the solution was flushed by nitrogen bubbling in the solution for *ca.* 30 min to remove any trace of bulk CO in the electrolyte. During this procedure, the electrode was held at 295 mV versus RHE, after which two cyclic voltammograms (CV) cycles were recorded under inert atmosphere at 10 or 50 mV s^{-1} from the hydrogen to the platinum oxide region (typically, between 45 and 1245 mV vs. RHE). The active area of platinum was then determined from the CO_{ad}-stripping peak coulometry, isolated by subtracting the 2nd cycle of the CV to the 1st one; this peak is usually located in the potential range from *ca.* 600 to 1000 mV vs. RHE. The calculation assumes a full monolayer of CO was adsorbed over platinum, which corresponds to 420 μC cm^{-2} [32]. The CAC double layer capacitance was calculated from the double layer current of the voltammograms, assuming the well admitted value: $C_{dl} = 10$ μF cm^{-2} [30]. From this value and knowing the mass of carbon for each electrode, we estimated the double layer (specific) area of the CAC samples (S_{dl}). We point out that although the value: $C_{dl} = 10$ μF cm^{-2} was measured for Vulcan XC72, we nevertheless assumed its validity for the CAC materials.

ORR kinetic parameters of the Pt/CAC materials were determined for oxygen-saturated electrolytes. For this purpose, we applied a permanent O_2 bubbling in the solution during the measurements to maintain O_2 concentration in the electrolyte at its saturation value. Before each linear quasi-steady-state voltammetry (1 mV s^{-1}), the working electrode was held for 1 min at 945 mV vs. RHE to ensure a reproducible platinum initial state of surface. We varied the RDE rotation speed from 500 to 4000 rpm to enable correction from oxygen diffusion–convection limitations using the well-known Levich theory [33]. The so-obtained ORR kinetic current density, $i_k = (i \times i_l)/(i_l - i)$ with i_l the limiting current and i the measured (experimental) current density (which is the function of the electrode potential), yields classical Tafel lines in the low current density region, from which we extract the Tafel slope (b) and the current density measured at 845 or 895 mV vs. RHE (i_{895}). From these values, we calculated the specific (SA_{845} or SA_{895}) ORR activities (current densities reduced to the active area of platinum).

3. Results and discussion

3.1. Thermogravimetric analysis and pyrolysis of the aerocellulose

Fig. 1 shows a typical thermogravimetric plot for aerocellulose, using the second TGA procedure (monotonous heating ramp of 2 °C min^{-1} from room temperature to 1200 °C). Table 1 presents the weight losses of the aerocellulose at various temperature intervals, obtained from the both thermogravimetric cycles. The first weight loss occurs either during the isothermal step at 40 °C, under vacuum for 0.5 h and Ar for 1.5 h (first TGA procedure) or below 180 °C (second TGA procedure). Below 180 °C, the sample typically loses 7–9 wt% of its initial mass, which mainly corresponds to water evaporation from the sample. The main weight loss occurs between 180 and 330 °C (*ca.* 71–72 wt%). According to Banyasz et al. [34], this loss corresponds to the formation of volatile species such as: CO, CO_2 and formaldehyde produced during the pyrolysis of cellulose. The total weight loss recorded during both TGA procedures is *ca.* 90%, whatever the cycle chosen. Cellulose being composed of 44.4% carbon, the theoretical mass loss should be much lower, *ca.* 55.6%, provided all the carbon remains and all the non-carbon species are volatilized. Our higher weight loss value suggests that some carbon species have volatilized during the pyrolysis, following C–C binding break, in agreement with some literature data [35]. Such high weight loss can result from evaporation of levoglucosan [36] and its subsequent degradation into volatile species like CO, CO_2, methanol, acetic acid, etc. [37,38]. These evolving O-containing gases (i.e. CO_2, CO, anhydro sugars, etc. [34,38,39]) could become *activators* for carbon combustion (thus acting as *combustion gases*), which will be discussed in Sections 3.2 and 3.3.

For all carbonized aerocellulose samples obtained from aerocellulose made from cellulose/NaOH/water gels and pyrolyzed (at 830 °C) as described in Section 2.4, the total weight loss after pyrolysis was 82.7% and 85.4% for CAC1 and CAC2, respectively, in agreement with what we expected from the TGA and literature data [35]. The total volume loss during pyrolysis, obtained by measuring the macroscopic dimensions of both aerocellulose samples before and after pyrolysis, reached *ca.* 90%. Nevertheless, the samples keep their monolithic initial shape after pyrolysis, as seen on the photographs of Fig. 2.

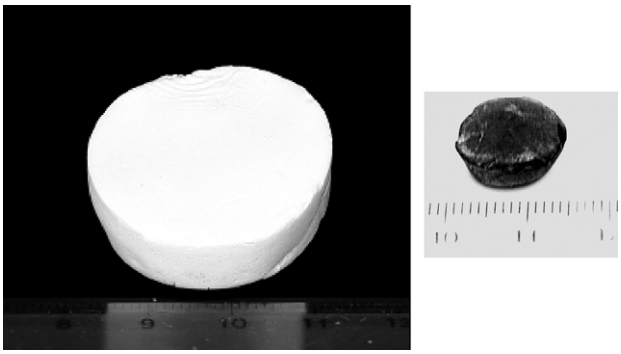

Fig. 2. Photographs of aerocellulose sample 1 before (AC1) and after (CAC1) pyrolysis. The magnification of both photographs is identical.

Table 2
Elemental composition of the two aerocellulose samples obtained from cellulose/NaOH/water gels before and after pyrolysis

Elemental composition	Average aerocellulose	Carbonized aerocellulose CAC1	Carbonized aerocellulose CAC2
wt% C	42 ± 2	90.8	88.6
wt% O	52 ± 2	4.30	4.47
wt% H	6 ± 0.5	1.07	1.92
Total	100	96.17	94.99

3.2. Elemental analysis of the carbonized aerocellulose

Elemental analyses of aerocellulose before and after pyrolysis were performed at the Service Central d'Analyse (CNRS, Vernaison, France). The results are summarized in Table 2. The amount of carbon is slightly higher for CAC1 than CAC2 (90.8 wt% vs. 88.6 wt%), while the hydrogen content is almost twice higher in CAC2 than CAC1 (1.92 wt% vs. 1.07 wt%). Both carbonized aerocellulose materials still present high quantities of oxygen (4.3–4.5 wt%) or hydrogen (1.07–1.92 wt%). This is a sign of an incomplete carbonization, despite the long duration of the pyrolysis cycle (see Section 2.4). Note that the total weights shown in Table 2 do not reach 100, which may result from the fact that the oxygen content measurement is sensitive to humidity, non-negligible humidity content (adsorbed water) being evidenced from TGA (see Fig. 1 and Table 1). Moreover, SEM-EDS or XPS spectra showed the presence of Na, K or Ca in the CAC2 sample (EDS ort XPS spectra not shown for the sake of brevity). This means that cellulose is adsorbing metal ions from tap water. The presence of such non-carbon elements within the CAC composition may influence their properties, as will be discussed in Section 3.3. Note that the presence of metal cations has already been shown to increase the pyrolysis effectiveness and lower the temperature at which the pyrolysis reaction occurs [40,41]. In Section 3.4, we will check whether the presence of metal ions in carbonized aerocellulose is detrimental to its potential use as electrocatalyst substrate for PEMFC applications. We nevertheless point out that the presence of such metal cations in CAC2 would probably be detrimental to the proton exchange membrane, if this material was to be used in PEMFC [42].

3.3. Porosity of the aerocellulose samples and their carbon counterparts

An example of aerocellulose and (platinum-free) carbonized aerocellulose morphology, observed by SEM, is shown in Fig. 3a and b, respectively. Corresponding TEM images are presented in Fig. 3c and d. The initial highly porous, *cloudy*, aerocellulose morphology becomes denser after pyrolysis, but still remains very porous. The density of pyrolyzed samples is in average three to four times higher than that of the initial aerocellulose (0.3–0.4 g cm^{-3} vs. 0.1–0.15 g cm^{-3}, respectively), in agreement with the overall aspect of the AC and CAC samples (see Fig. 2). There is practically no difference between the aerocellulose and the corresponding carbonized aerocellulose structures, as seen by TEM, at the level of mesoporosity.

In these preparation conditions, the shape of AC1 and AC2 (before pyrolysis) pore size distribution, obtained from mercury porosimetry, is essentially identical. Therefore, only the data for AC2 are presented on Fig. 4. The pore size distribution for AC2 (and AC1) is obviously bimodal, with macropores and mesopores diameters

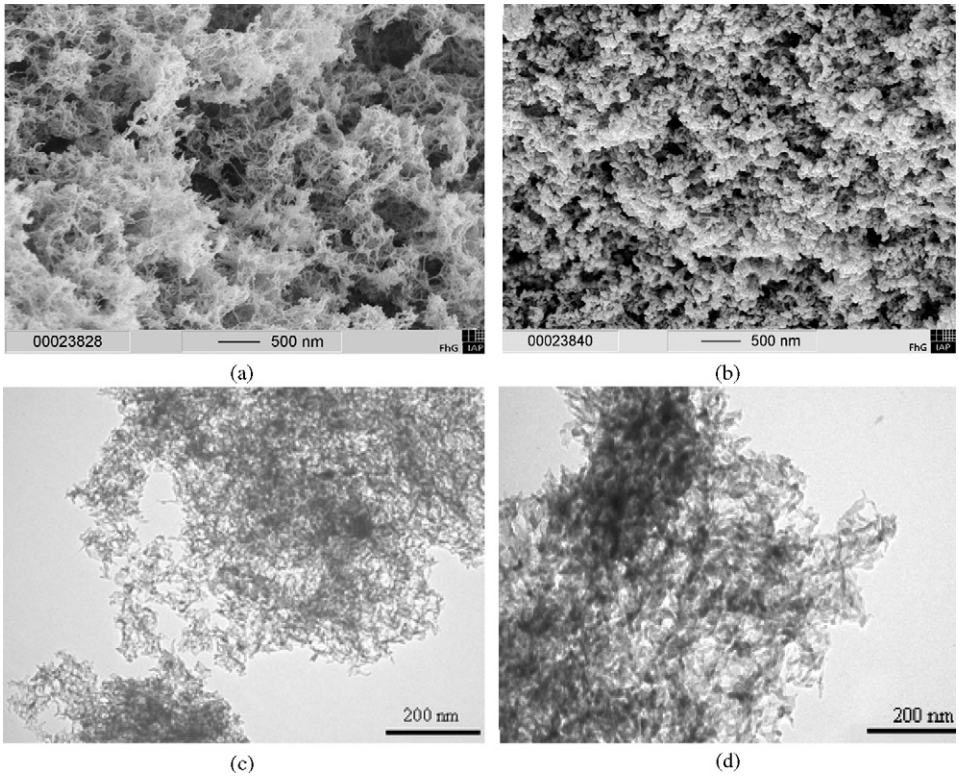

Fig. 3. SEM images of aerocellulose AC1 (a) and its carbon counterpart CAC1 (b); TEM images for AC2 (c) and CAC2 (d).

Table 3
Effect of the thermal activation treatment on the CAC1 weight loss (upon activation) and active (double layer) areas and resulting platinum active areas and ORR kinetic parameters for Pt/CAC1 as well as the benchmark commercial (E-TEK) 20 wt% Pt/Vulcan XC72 sample

Sample	Activation	Weight loss (%)	S_{dl} ($m^2\,g^{-1}$)	$S_{Pt\text{-}CO}$ ($m^2\,g^{-1}$)	b ($mV\,dec^{-1}$)	SA_{845} ($\mu A\,cm^{-2}$ Pt)	SA_{895} ($\mu A\,cm^{-2}$ Pt)	MA_{845} ($A\,g^{-1}$ Pt)	MA_{895} ($A\,g^{-1}$ Pt)
Pt/CAC1	1 h, 700 °C	7	410 ± 10	4.1 ± 0.1	−74 ± 0.5	150 ± 1.0	35	6.2	1.4
	1 h, 800 °C	13	450 ± 120	8.9 ± 0.4	−74 ± 2	130 ± 16	33 ± 2.5	11	3.0
	1 h, 900 °C	50	690 ± 140	7.7 ± 0.8	−79 ± 3	130 ± 17	36 ± 6.1	10	2.80
	Raw	–	560 ± 7.5	4.1 ± 0.2	−85	97	28	4.0	1.1
Pt/Vulcan XC72	E-Tek	–	–	72	−70	–	31	–	43

centered on *ca.* 500 and 30–40 nm, respectively. The pyrolysis basically shifts the distribution towards smaller pore size values, but seemingly in a different way for the two samples. On the one hand for CAC1, macropores of *ca.* 100 nm and mesopores of 30–40 nm diameter are observed. The bimodal pore distribution is conserved upon pyrolysis. CAC2 only exhibits small macropores of *ca.* 100-nm diameter, and the bimodal pore distribution seems to be lost. It is worth noting here that mercury porosimetry is only valid for mesopores and small macropores of diameter greater than 7.5 nm [5,6,16]. Smaller pores are presumably useless regarding PEMFC electrocatalysts, since they do not enable facile reactant/product (e.g. O_2 and H_2O, respectively) transport to/from the active sites [5,6,43]. We assume that, the bimodal pore distribution could have also been conserved for CAC2, with generation of pores smaller than 7.5-nm diameter, not detectable from Hg porosimetry. This complex behavior for CAC2 may be associated to the exhaust of the *combustion gases* mentioned in Section 3.1. These gases likely originate from the bulk of the samples in the course of their pyrolysis, and their concentration in oxidizing components (e.g. H_2O, CO_2, CO, CH_2O [36–38,40]) may increase as they evolve out of the sample, yielding the cracking of C–C bonds within the cellulose network and the concomitant creation of carbonyl groups [40], hydrocarbons [44], hydrogen or methane [39,40,44]. Thus, the evolution of such gaseous species could yield small macropores with detriment to mesopores. Macropores have indeed been evidenced by mercury porosimetry. The possible presence of metal cations in AC2 (see Section 3.2), likely enhances this phenomenon [40,41,44]. The pyrolysis could also start at lower temperature in AC2 (favored by the presence of metal cations), giving more time to the carbon network to reorganize during the heat treatment. As a result, meso- or micropores (diameter below 7.5 nm) would be generated for CAC2. This latter hypothesis goes in line with the fact that (i) both CAC samples exhibit specific area beyond 400 $m^2\,g^{-1}$, as measured from electrochemistry (see the double layer areas: S_{dl} in Table 3), and that (ii) such high specific area cannot be reached only with the macropores (*ca.* 100-nm diameter) detected from Hg porosimetry for CAC2. This indirectly demonstrates the presence of small mesopores (or even micropores) for CAC2. Note that such high specific area (especially for diameter above *ca.* 10 nm, which are compatible with low mass-transport hindrance to/from the active sites) is suitable for reaching high dispersion for the platinum nanoparticles onto the CAC surface [5,6,11].

3.4. Influence of impurities on the surface of carbonized aerocellulose on platinum insertion

The elemental analysis (see Section 3.2) revealed that non-carbon elements are not negligible within the CAC composition. These may either be located in the bulk of the carbonized aerocellulose structure or on the surface. In order to check the nature of the surface groups from both CAC samples, we performed IR spectroscopy on both materials before and after the thermal activation. Fig. 5 shows that the raw (non-activated) CAC samples display higher amounts of oxygenated surface groups. Such surface groups can be partly eliminated by thermal activation (preceding Pt insertion procedure): after such activation, some of the OH and CO groups (the nature of which was extensively studied in Ref. [15]) disappear, as clearly seen on Fig. 5, which shows a wide band appearing in the range 1400–1100 cm^{-1}. This likely results from the cleaning of the CAC surface from oxide surface groups, e.g. carbonyl surface groups [15], as also evidenced for the same activation treatment of carbon blacks [45]. Thus, the raw CAC surface is probably covered by oxygenated species, e.g. carbonyl groups, the production of which has been shown to increase during pyrolysis when alkali metal cations are present [40], in agreement with CAC2 elemental composition (see Section 3.2).

Sections 3.2 and 3.3 showed that it was possible to prepare two CAC samples bearing rather identical physical parameters (e.g. pore size distribution, specific area). We studied these two samples for platinum insertion, using the same techniques of Pt impregnation/reduction and characterization of the Pt specific area. Despite the very small apparent differences between these two carbon materials, it appears that electrochemical experiments in electro-

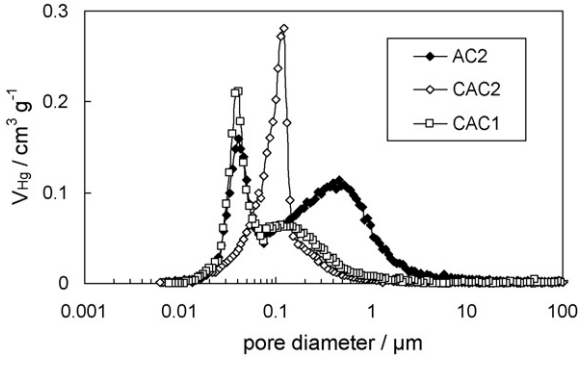

Fig. 4. Pore size distribution obtained from mercury porosimetry for AC2, CAC1 and CAC2 samples.

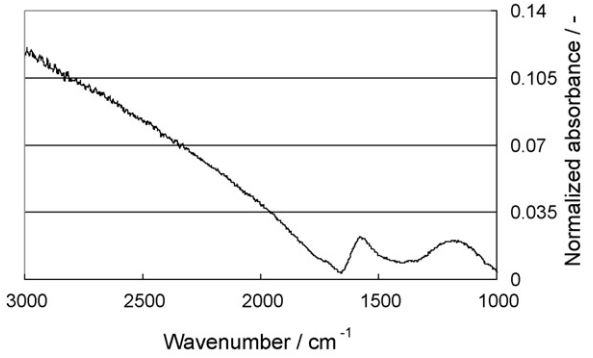

Fig. 5. Normalized IR absorption spectra $(A_{raw} - A_{ativated})/A_{raw}$ showing the influence of the thermal activation treatment (1 h at 800 °C; CO_2 atmosphere) on CAC2 surface chemistry.

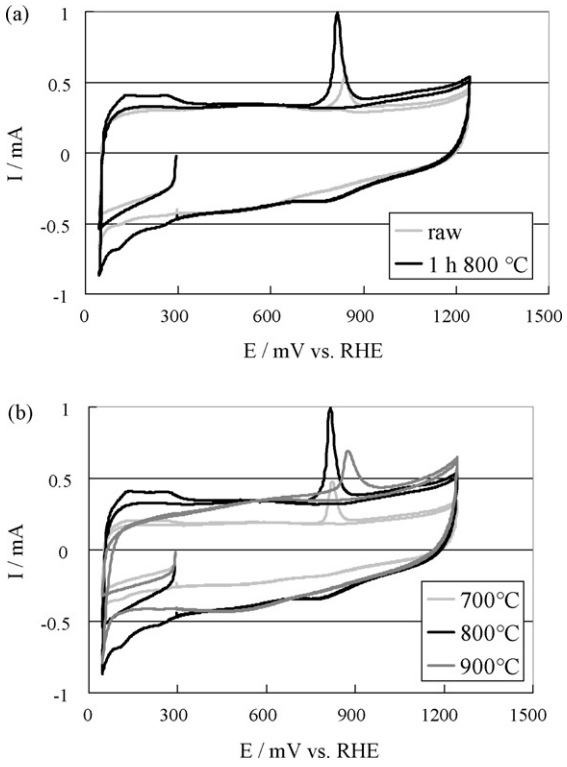

Fig. 6. Comparison of raw and activated (1 h, 800 °C) samples (a) and influence of the activation temperature (b) on the CO_{ad}-stripping voltammograms for Pt/CAC1 sample—1 M H_2SO_4, 25 °C, 50 mV s^{-1}.

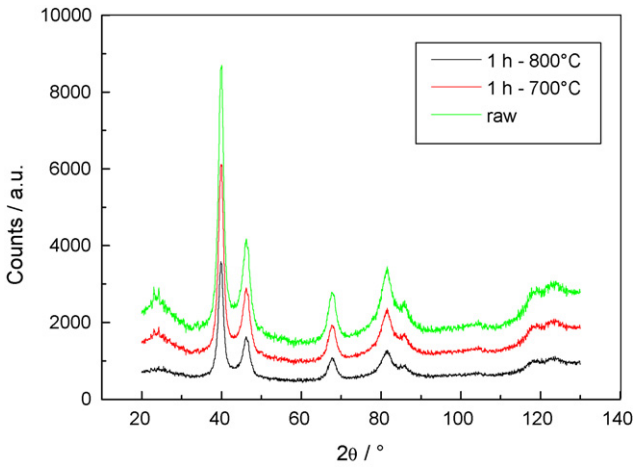

Fig. 7. XRD spectra for the Pt/CAC1 samples obtained without or with an activation (thermal) treatment of the CAC1 material.

catalysis require the maximum surface cleanness possible: even after activation, the Pt insertion could not be optimized for the CAC2 sample. Although it has been possible to deposit Pt nanoparticles over CAC2, these were blocked by poison adsorbates (metal cations, strongly adsorbing anions (e.g. Cl^-) or organic impurities). This was particularly detected during CO_{ad}-stripping experiments, for which the second cycle showed the absence of any hydrogen desorption feature from the Pt/CAC2 nanoparticles (curves not shown for brevity). As discussed in Ref. [11], CO is strongly adsorbed over Pt, which can yield to pollution displacement. However, this pollution is not eliminated (just displaced by CO_{ad}) and may diffuse back to the Pt particles upon CO_{ad}-stripping, thus inhibiting any Pt activity (and particularly H-adsorption/desorption).

On the contrary, the CO_{ad}-stripping from Pt/CAC1 (Fig. 6) exhibits the expected shape for carbon-supported Pt nanoparticles (see for example Refs. [11,32,46]). Because of the difficulties regarding the use of CAC2, we focused on CAC1 to investigate the optimal experimental conditions to deposit Pt nanoparticles.

We studied the impact of the CAC1 thermal activation on the possibility to deposit Pt nanoparticles at its surface. While no activation yields poor Pt insertion (the surface chemistry is then complex and prevents $PtCl_6^{2-}$ adsorption), 1-h activation at 800 °C (i.e. a temperature close to the CAC final pyrolysis temperature) yields much better results (Fig. 6a).

Knowing that a thermal activation step is beneficial, we attempted to determine the most suitable activation temperature. Fig. 6b and Table 3 show that the highest active area of platinum (determined from CO_{ad}-stripping coulometry) is obtained for 1 h activation at 800 °C, compared to 700 and 900 °C. A likely reason is that at 700 °C the surface *cleaning* brought by the activation is not sufficient (i) to enable the anionic platinum adsorption from chloroplatinic acid impregnation and (ii) to open the microporosity [45]. $PtCl_6^{2-}$ adsorption is indeed known to be favored for carbon substrates free of oxygenated surface groups [47–50]. As a result, less carbon surface is available for Pt salt adsorption, resulting in lower active area of platinum. The *ca.* 2 times lower double layer current for CAC1 activated at 700 °C (compared to the two other samples) agrees with such hypothesis. Conversely at 900 °C, the surface *cleaning* and porosity opening are probably more efficient. However, such harsh thermal activation, which is known to open and widen the narrow microporosity [51], may destruct the internal CAC structure; such process is more severe at high burn off rates (*ca.* above 50 wt% loss) and/or activation temperature typically above 900 °C [52]. The high weight loss upon activation at 900 °C (Table 3) is consistent with the results reported in the literature.

We completed these observations by a morphological study of the Pt nanoparticles using XRD (Fig. 7) and TEM (Fig. 8) for the Pt/CAC materials. Both XRD and TEM data reveal (i) the little graphitization of the CAC samples and (ii) the very mild influence of the activation step on the Pt particles morphology. The average Pt crystallite sizes, determined from XRD (Fig. 7), hardly varies with the activation treatment: they are, respectively 4.1, 4.0 and 5.2 nm for the 1 h, 800 °C; 1 h, 700 °C and raw Pt/CAC samples. These crystallites sizes agree with those of the individual particles detected in high-resolution TEM (Fig. 8, lower right picture). However, all TEM pictures of Fig. 8 show these crystallites are essentially agglomerated into larger clusters of *ca.* 20 nm or more (the cluster size varies with the samples). Such extent of agglomeration renders meaningless any attempt to determine particle size distribution histograms. It can result both from the rather high coverage in surface oxide groups on all CAC samples and the method of reduction of the adsorbed Pt salt (in aqueous solution of BH_4^-). Fig. 8 nevertheless confirms that 1 h-800 °C is probably the more appropriate activation treatment performed in the present case, since the agglomerates are more open (less dense and thus accessible from the electrochemical point of view). We nevertheless realize that even the Pt/CAC 1 h-800 °C is not at all yet competing with the commercial materials, which is confirmed by the *ca.* 10 times lower MA values of all Pt/CAC samples in Table 3.

The slight decrease of the contact angles with activation temperature increase (Table 4) shows that CAC1 becomes mildly more hydrophilic upon activation, as long as the activation temperature remains below that of the pyrolysis (i.e. 800 °C). This is surprising as one would expect that further heat treatment (under CO_2) *cleans* the surface, but confirms the TEM observations. It should be noted

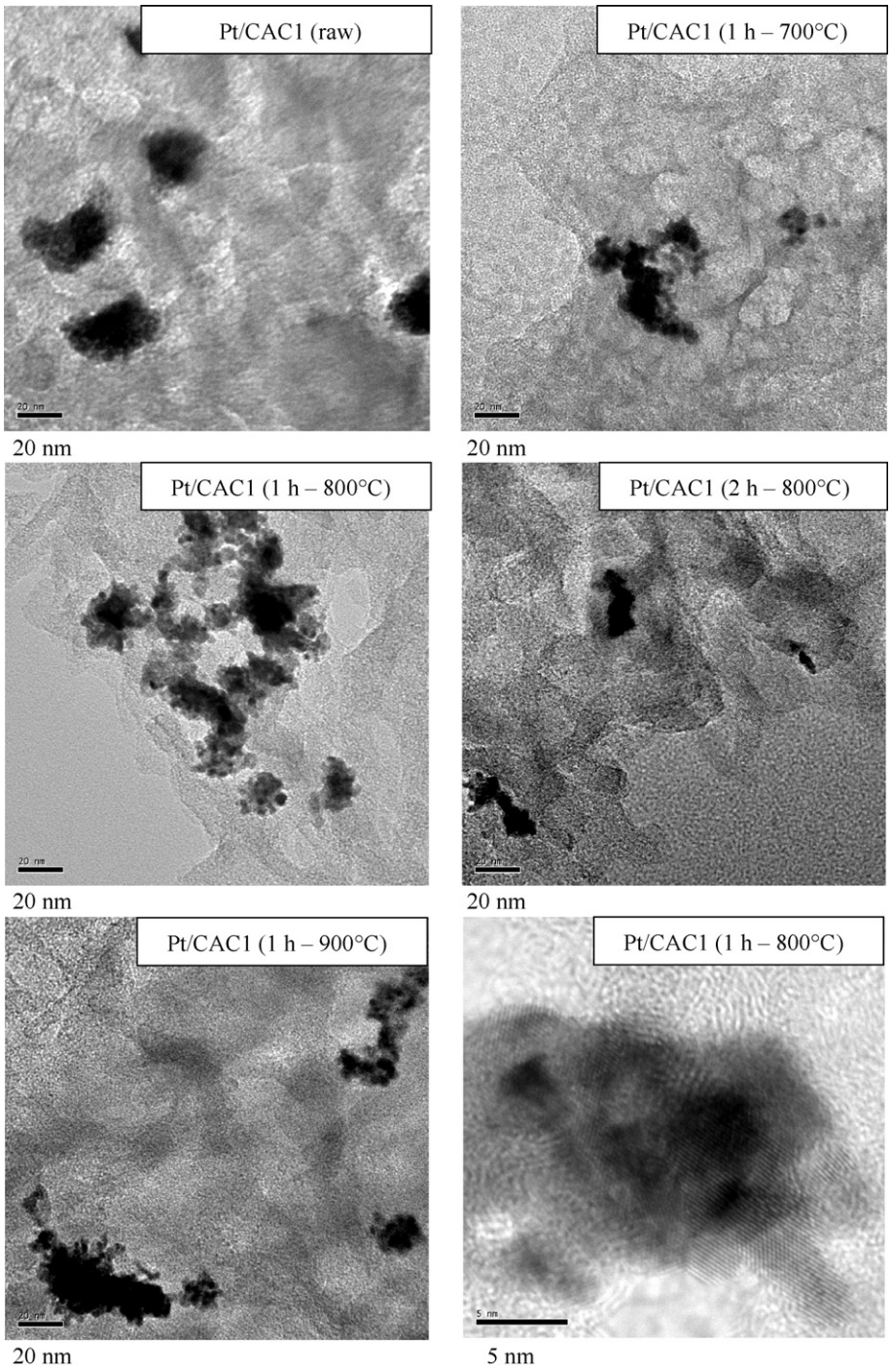

Fig. 8. TEM images for the Pt/CAC1 samples obtained without or with an activation (thermal) treatment of the CAC1 material.

Table 4
Hydrophilicity tests for CAC1 performed for 15 μL water drop under water-saturated atmosphere at 21 °C; the contact angle of the water drop was measured right upon the drop deposition

Activation	Contact angle (°)
Raw	150 ± 2
1 h, 700 °C	149 ± 0
1 h, 800 °C	143 ± 0.4
1 h, 900 °C	–

that the surface of CAC1 activated at 900 °C was so hydrophobic that any measurement of the contact angle was impossible. These data confirm that activation below the pyrolysis temperature has a very little impact on the CAC surface properties. On the contrary, activation at temperature above pyrolysis temperature impacts more dramatically both the surface properties and the CAC morphology (the pyrolysis indeed continues), as already observed for carbon aerogels elaborated from the cellulose acetate route [15]. As a consequence, it is probably wiser to avoid any activation step. Previous studies on carbon aerogel from the resorcinol–formaldehyde route [5,6,11] showed an activation step after pyrolysis is not nec-

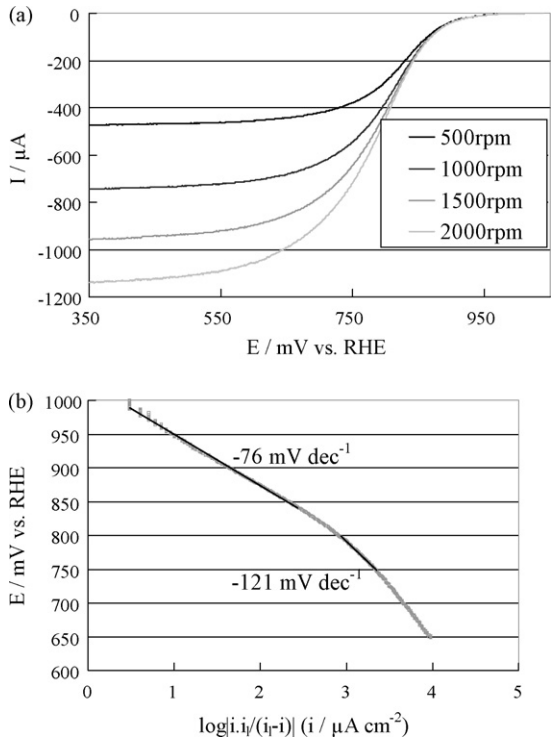

Fig. 9. Quasi-steady-state voltammograms (a) and related Tafel slopes (b) for ORR on Pt/CAC1 activated for 1 h at 800 °C—1 M H_2SO_4, 25 °C, 1 mV s^{-1}.

essary when higher pyrolysis temperature is used (*ca.* 1050 °C). One can think that nanostructured carbons from the cellulose route would not need any thermal activation step, provided their pyrolysis temperature is high enough to yield sufficiently *clean* CAC materials (e.g. above 1000 °C, see Refs. [5,6,11]). This topic is beyond the scope of the present paper, but will be studied in the future.

3.5. Oxygen reduction reaction kinetics for Pt/CAC1

As shown above, the best procedure of carbon aerocellulose treatment we found (for CAC materials obtained from pyrolysis at 800 °C) is to activate CAC1 at 800 °C for 1 h under CO_2 atmosphere. We nevertheless investigated the raw and activated CAC1 materials towards the oxygen reduction reaction. Fig. 9a shows typical quasi-steady-state ORR voltammograms obtained in the porous-RDE configuration [19,20]. They exhibit plateaus demonstrating oxygen diffusion–convection limitation at high ORR overpotential. Using the Levich theory, we calculated the ORR current densities corrected from O_2 diffusion in solution [33] and plotted them in the Tafel plane (Fig. 9b). From this plot, we extract the ORR kinetic parameters (Tafel slope in the low current density region: *b* and specific activities: SA_{845} or SA_{895}), which are summarized in Table 3. The results show that whatever the activation procedure, Pt/CAC1 samples exhibit smaller mass activities than the commercial Pt/Vulcan XC72 electrocatalyst. However, they show comparable or slightly higher ORR specific activities to that for our benchmark (commercial) 20 wt% Pt/Vulcan XC72 sample. This highlights the benefit of using such *green* materials as electrocatalyst support for Pt nanoparticles, provided their elaboration procedure prevents any surface pollution. Nevertheless, more work is needed to optimize the Pt/CAC materials, both from the CAC state of surface (oxide group content) prospective and from the platinum deposition procedure.

4. Conclusions

Nanostructured carbonized aerocellulose elaborated from pyrolysis of aerocellulose display high specific areas (above 400 m^2 g^{-1}). Their carbon content after such pyrolysis (at 830 °C under nitrogen flow) is below 91%, albeit their weight loss upon pyrolysis exceeded 80 wt%. These nanostructured new carbon materials display very complex surface chemistry and require (i) rather clean elaboration precursors, media and processes and (ii) an additional thermal activation treatment (in CO_2 atmosphere), to enable efficient Pt insertion. The thermal activation parameters have been studied in order to attempt optimizing the Pt/CAC materials. However, no thermal treatment studied appears enough to optimize our Pt/CAC materials: the Pt particles are mostly agglomerated, possibly resulting from the large amount of surface oxide groups over CAC. The amount of platinum deposited onto the CAC is significant although the experimental conditions still need improvement. We believe higher pyrolysis temperature should yield better aerocellulose carbonization and thus facilitate the Pt/CAC elaboration process. The ORR activities obtained with the Pt/CAC materials are promising in term of specific activities, since they are comparable with that of similar Pt/carbon black electrocatalysts. However, the mass activities are still low, as a result of the Pt particles agglomeration and resulting low specific surface area of platinum. Provided their surface properties are improved, these *green* cellulose-based nanostructured carbons could be interesting electrocatalyst supports for Pt nanoparticles in PEMFC applications.

Acknowledgements

The authors thank the European Commission for financial support (project “Aerocell”, No. NMP3-CT2003-505888). They also gratefully acknowledge M. Pinnow and H.-P. Fink (FhG-IAP, Golm, Germany) for performing the SEM images, B. Simon (SAFT, Bordeaux, France) for the mercury porosimetry measurements, M.-Y. Perrin (CEMEF, Sophia-Antipolis, France) for the TEM images, P. Ilbizian (CEP, Sophia Antipolis, France) for the supercritical drying, S. Brice-Profeta (SIMAP, Grenoble, France) for her help in the thermogravimetric analysis and S. Coindeau (CMTC, Grenoble, France) for the XRD analyses of the Pt/CAC samples.

References

[1] W. Vielstich, A. Lamm, H.A. Gasteiger, Handbook of Fuel Cells, Wiley, Chichester, 2003.
[2] J.-B. Donnet, A. Voet, Carbon Black, Marcel Dekker, New York, 1976.
[3] X. Lu, O. Nilsson, J. Fricke, R. Pekala, J. Appl. Phys. 73 (1993) 581.
[4] H. Tamon, H. Ishizaka, M. Mikami, M. Okazaki, Carbon 35 (1997) 791.
[5] J. Marie, S. Berthon-Fabry, M. Chatenet, E. Chainet, R. Pirard, N. Cornet, P. Achard, J. Appl. Electrochem. 37 (2007) 147.
[6] J.F. Marie, S. Berthon-Fabry, P. Achard, M. Chatenet, E. Chainet, R. Pirard, N. Cornet, ECS Trans. 1 (2006) 509.
[7] R.W. Pekala, J.C. Farmer, C.T. Alviso, T.D. Tran, S.T. Mayer, J.M. Miller, B. Dunn, J. Non-Cryst. Solids 225 (1998) 74.
[8] C. Moreno-Castilla, F.J. Maldonado-Hodar, Carbon 43 (2005) 455.
[9] M. Glora, M. Wiener, R. Petricevic, H. Probstle, J. Fricke, J. Non-Cryst. Solids 285 (2001) 283.
[10] R. Petricevic, M. Glora, J. Fricke, Carbon 39 (2001) 857.
[11] J. Marie, S. Berthon-Fabry, P. Achard, M. Chatenet, A. Pradourat, E. Chainet, J. Non-Cryst. Solids 350 (2004) 88.
[12] A. Smirnova, X. Dong, H. Hara, A. Vasiliev, N. Sammes, Int. J. Hydrogen Energy 30 (2005) 149.
[13] W.S. Baker, J.W. Long, R.M. Stroud, D.R. Rolison, J. Non-Cryst. Solids 350 (2004) 80.
[14] H. Jin, Y. Nishiyama, M. Wada, S. Kuga, Colloids Surf. A: Physicochem. Eng. Aspects 240 (2004) 63.
[15] E. Guilminot, F. Fischer, M. Chatenet, A. Rigacci, S. Berthon-Fabry, P. Achard, E. Chainet, J. Power Sources 166 (2007) 104.
[16] F. Fischer, A. Rigacci, R. Pirard, S. Berthon-Fabry, P. Achard, Polymer 47 (2006) 7636.

[17] R. Gavillon, Preparation and characterization of ultra-porous cellulose material, in Ph.D. Thesis, ENSMP, Sophia-Antipolis, France, 2007.
[18] R. Gavillon, T. Budtova, Biomacromolecules 9 (2008) 269.
[19] F. Gloaguen, F. Andolfatto, R. Durand, P. Ozil, J. Appl. Electrochem. 24 (1994) 863.
[20] A. Gamez, D. Richard, P. Gallezot, F. Gloaguen, R. Faure, R. Durand, Electrochim. Acta 41 (1996) 307.
[21] C. Orr, J.M. Dallavalle, Fine Particle Measurement—Size, Surface, and Pore Volume, Mac Millan, New York, 1959.
[22] J. Rouquerol, D. Avnir, C.W. Fairbridge, D.H. Everett, J.H. Haynes, N. Pernicone, J.D.F. Ramsay, K.S.W. Sing, K.K. Unger, Pure Appl. Chem. 66 (1994) 1739.
[23] J.C. Groen, L.A.A. Peffer, J. Perez-Ramirez, Characterization of Porous Solids Vi (2002) 91.
[24] C. Roy, T. Budtova, P. Navard, Biomacromolecules 4 (2003) 259.
[25] A. Bisson, A. Rigacci, D. Lecomte, E. Rodier, P. Achard, Dry. Technol. 21 (2003) 593.
[26] G.M. Pajonk, Proceedings of the 2nd International Symposium on Aerogels, Montpellier, France, 1989, p. 13.
[27] M.J. van Bommel, A.B. de Haan, J. Non-Cryst. Solids 186 (1995) 78.
[28] P.H. Tewari, A.J. Hunt, K.D. Lofftus, Mater. Lett. 3 (1985) 363.
[29] K. Kinoshita, in: S. Sarangapani, J.R. Akridge, B. Schumm (Eds.), The Electrochemistry of Carbon, The Electrochemical Society, Cleveland, OH, U.S., 1983, p. 273.
[30] K. Kinoshita, Carbon, Electrochemical and Physicochemical Properties, John Wiley & Sons, New York, 1988.
[31] E. Guilminot, A. Corcella, F. Charlot, F. Maillard, M. Chatenet, J. Electrochem. Soc. 154 (2007) B96.
[32] E. Guilminot, A. Corcella, M. Chatenet, F. Maillard, J. Electroanal. Chem. 599 (2007) 111.
[33] A.J. Bard, L.R. Faulkner, Electrochemical Methods, John Wiley & Sons, Inc., Weinheim, 2001.
[34] J.L. Banyasz, S. Li, J. Lyons-Hart, K.H. Shafer, Fuel 80 (2001) 1757.
[35] J.A. Lie, M.B. Hagg, J. Membr. Sci. 284 (2006) 79.
[36] M. Essig, G.N. Richards, E. Schenck, Mechanism of Formation of the Major Volatile Products from Pyrolysis of Cellulose, Wiley Interscience, New York, 1989, p. 841.
[37] O. Ishida, D.-Y. Kim, S. Kuga, Y. Nishiyama, J. M. Brown, Cellulose 11 (2004) 475.
[38] R. Alen, E. Kuoppala, P. Oesch, J. Anal. Appl. Pyrolysis 36 (1996) 137.
[39] R. Radmanesh, Y. Courbariaux, J. Chaouki, C. Guy, Fuel 85 (2006) 1211.
[40] C.Y. Yang, X.S. Lu, W.G. Lin, X.M. Yang, J.Z. Yao, Chem. Res. Chin. Univ. 22 (2006) 524.
[41] P.T. Williams, P.A. Horne, Renew. Energy 4 (1994) 1.
[42] C. Iojoiu, E. Guilminot, F. Maillard, M. Chatenet, J.Y. Sanchez, E. Claude, E. Rossinot, J. Electrochem. Soc. 154 (2007) B1115.
[43] M. Uchida, Y. Fukuoka, Y. Sugawara, N. Eda, A. Ohta, J. Electrochem. Soc. 143 (1996) 2245.
[44] B.I. Park, J.W. Bozzelli, M.R. Booty, Ind. Eng. Chem. Res. 41 (2002) 3526.
[45] O. Antoine, in Ph.D. Thesis, INPG, France, Grenoble, 1998.
[46] O. Antoine, R. Durand, J. Appl. Electrochem. 30 (2000) 839.
[47] P.L. Antonucci, V. Alderucci, N. Giordano, D.L. Cocke, H. Kim, J. Appl. Electrochem. 24 (1994) 58.
[48] F. Rodriguez-Reinoso, Carbon 36 (1998) 159.
[49] S.R. de Miguel, O.A. Scelza, M.C. Roman-Martinez, C. Salinas-Martinez de Lecea, D. Cazorla-Amoros, A. Linares-Solano, Appl. Catal. A: Gen. 170 (1998) 93.
[50] M.C. Roman-Martinez, D. Cazorla-Amoros, A. Linares-Solano, C. Salinas-Martinez de Lecea, Curr. Top. Catal. 1 (1997) 17.
[51] F. Rodriguez-Reinoso, M. Molina-Sabio, M.T. Gonzalez, Carbon 33 (1995) 15.
[52] A. Ahmadpour, D.D. Do, Carbon 34 (1996) 471.